Translational Disturbance Rejection for Jet-Actuated Flying Continuum Robots on Mobile Bases

Yukihiro Maezawa, Yuichi Ambe ⓘ, *Member, IEEE*, Yu Yamauchi ⓘ, *Member, IEEE*, Masashi Konyo ⓘ, *Member, IEEE*, Kenjiro Tadakuma ⓘ, *Member, IEEE*, and Satoshi Tadokoro ⓘ, *Fellow, IEEE*

Abstract—Although continuum robots have the potential to operate in narrow areas by changing their shapes and propelling their bodies, they easily vibrate under sudden or periodic applications of external forces. Suppressing vibrations is difficult in our jet-actuated continuum robot because the movements of its mobile base cannot be controlled with the same system as the movements of the robot, and mobile base oscillation increases the risk of resonance. In this study, a disturbance rejection was realized for the Dragon Firefighter, a jet-actuated flying continuum robot on a mobile base, for rapid and safe fire extinguishing using a 4-m-long flying fire hose consisting of two nozzle units and flexible hoses. An $\mathscr{H}_\infty$-based disturbance-rejection controller was designed to suppress the vibration of the head nozzle unit posture against the acceleration of the mobile base. Then, the robot parameters were identified from tensile tests and dynamic excitation experiments. Dynamic simulations confirmed that the controller reduced the peak gain of the frequency response by approximately 2 dB for various robot shapes. Robot experiments confirmed that the proposed method reduced the peak gain of the frequency response by approximately 3 dB, which increased the extra injection range of the nozzle by approximately 16%.

Index Terms—Aerial systems: Mechanics and control, continuum robots, flexible robotics, fluid jet, motion control.

I. INTRODUCTION

CONTINUUM robots can potentially be used to gather information as they can operate in narrow areas by changing their shapes and propelling their bodies. Various driving mechanisms have been proposed for manipulating the flexibility of bodies [1]. For example, tendon-driven continuum robots

Yukihiro Maezawa, Masashi Konyo, and Satoshi Tadokoro are with the Graduate School of Information Sciences, Tohoku University, Sendai 980-8577, Japan (e-mail: maezawa.yukihiro@rm.is.tohoku.ac.jp; konyo@rm.is.tohoku.ac.jp; tadokoro@rm.is.tohoku.ac.jp).

Yuichi Ambe is with the Graduate School of Engineering Science, Osaka University, Osaka 565-0871, Japan (e-mail: ambe.yuichi.es@osaka-u.ac.jp).

Yu Yamauchi is with the Graduate School of Systems Science and Technology, Akita Prefectural University, Yurihonjo 010-0195, Japan (e-mail: yamauchi.yu@akita-pu.ac.jp).

Kenjiro Tadakuma is with Tough Cyberphysical AI Research Center, Tohoku University, Sendai 980-8577, Japan (e-mail: tadakuma@rm.is.tohoku.ac.jp).
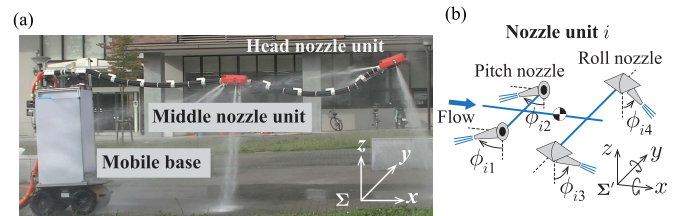
Fig. 1. 4m-long jet-actuated flying continuum robot with a mobile base ((a) Robot and (b) Structure of nozzle unit i).

change shape by pulling wire threads along their backbone. Pneumatic-driven continuum robots [2] change shape using multiple distributed pneumatic actuators. Concentric tube continuum robots extend and change shapes using multiple concentric tubes with different stiffness values. Torus-shaped structures for extension and steering were also proposed [3]. Jet-actuated continuum robots that can directly generate translational forces to steer and propel through expelling fluid jets have recently been developed [4], [5], [6], [7].

However, these continuum robots can easily vibrate under a sudden or periodic application of external forces. This is because their bodies are long and flexible. Under vibration, it is difficult to precisely control the shape and position. To date, several vibration-damping methods have been proposed, such as vibration suppression by controlling the displacement of wires threaded through the body [8], active vibration control using fuzzy logic and neural networks [9], a damping method using the effect of flowing water [10] and a damping mechanism using threaded wires and rotary dampers [11]. However, these studies did not consider the movement or oscillation of the robot's base.

Consequently, we have developed Dragon Firefighter (DFF), a jet-actuated continuum robot with a mobile base (Fig. 1(a)), which faces body vibrations, mainly caused by mobile base movements and oscillations. The DFF is used for rapid and safe fire extinguishing using a 4-m-long flying fire hose consisting of two nozzle units and flexible hoses. The robot flies and changes its shape using the reaction forces generated by multiple water jets, and is propelled forward with a mobile base. Because the DFF is designed to work in fire-extinguishing situations, the end of the DFF can be connected to the top of a conventional fire-ladder truck as a mobile base or to a long rigid pipe to extend its insertion length. In these cases, vibration suppression in the DFF is challenging for two reasons. First, the long aerial ladder and pipe vibrations can cause unintended resonance. Because the moving ranges of injection nozzles are limited, severe vibrations of the nozzle units can cause saturation of the reaction forces

in jet-actuated continuum robots, resulting in a fall. Second, we cannot utilize control inputs and sensing values from the mobile base for the vibration suppression because we assume conventional fire-ladder trucks as candidates of the mobile base.

Therefore, this study aims to realize disturbance rejection in the DFF without the control inputs and sensing values of the mobile bases. This study focuses on front-back direction disturbances because the mobile base mainly moves longitudinally. First, a two-dimensional (2D) model is created considering the base. Subsequently, a disturbance-rejection controller is designed using the $\mathcal{H}_\infty$ controller [12] to suppress the vibration of the head nozzle unit caused by the acceleration of the base. The robot parameters are identified from tensile tests and dynamic excitation experiments, and the proposed controller is verified using simulations and experiments of an actual 4-m-long continuum robot. This method can decrease the vibration amplitude and increase the nozzle injection range.

II. RELATED WORKS

Several studies have focused on the vibration suppression of mobile manipulators or drones. Pradeep et al. [13] used a resonance ratio control-based null space controller to suppress the vibration of an inverted pendulum arm mounted on a two-wheel mobile manipulator. Bernt et al. [14] proposed a method for improving the positioning accuracy and vibration suppression of a two-link flexible manipulator on a moving platform using an onboard camera image. Rigotti-Thompso et al. [15] applied an $\mathcal{H}_\infty$-based disturbance-rejection controller to a wheeled mobile manipulator that runs on uneven terrain to eliminate terrain disturbances that affect the end-effector attitude. Huynh et al. [6] applied an $\mathcal{H}_\infty$-based disturbance-rejection controller for a water-jet-actuated drone to deal with the hose effect. Although we adopted the $\mathcal{H}_\infty$-based approach to suppress the vibrations, this is the first study to apply it to mobile jet-actuated continuum robots. In contrast to manipulators or drones, additional efforts are required for modeling and parameter identification owing to the flexibility of continuum robots.

III. TARGET ROBOT AND PROBLEM FORMULATION

A. Target Robot Configuration

1) Entire Robot: As shown in Fig. 1(a), the targeted robot DFF was approximately 4 m long with a mobile base. The robot consisted of two nozzle units and a flexible body. The two nozzle units were located at the head and middle of the robot. The body consisted of a corrugated tube, inside which cables and a water tube were located. Water pressurized by a pump flowed through the hose and was expelled from each nozzle unit to generate the force required for floating. The shape of the body (including the position and velocity of each nozzle unit) was estimated using inertia measurement units (IMU, acquiring rate: 1000 Hz) attached to the outside of the body every 400 mm, as in [16].

2) Nozzle Unit: Each nozzle unit $i(i = 1, 2)$ contained four active rotating nozzles. The positions of the rotating nozzles are shown in Fig. 1(b). The unit had two pairs of rotating nozzles that rotated around the pitch and roll axes. The angles of the nozzles, determined to realize the target net force, were defined as ϕ_{i1-i4}, and they are explained in Section III-B.

3) Mobile Base: The robot's end was attached to an active cart (HUSKY A200, *Clearpath Robotics Inc.*) via a tower with an aluminum frame (approximately 1.6 m height). This cart was

operated remotely, had a mass of 50 kg, and was controlled by velocity input (maximum speed of 1.0 m/s).

B. Conventional Flight Control for the DFF With a Fixed End

We previously proposed a simple controller for the DFF with a fixed end [16], [17]. The net force vector $\boldsymbol{f}_i$ of each nozzle unit $i(i = 1, 2)$ was controlled as follows:

$$\boldsymbol{f}_i = \boldsymbol{F}_i - D_i \dot{\boldsymbol{r}}_i, \tag{1}$$

where $\boldsymbol{F}_i$ denotes a constant force vector that determines the shape of the robot (equilibrium point); $-D_i \dot{\boldsymbol{r}}_i$ is a damping term for the nozzle movement, which contributes to increasing convergence speed; $\dot{\boldsymbol{r}}$ is the velocity vector of nozzle unit i; and $D_i = \mathrm{diag}(s_x, s_y, s_z)$ is the coefficient matrix of the damping term. All the vectors are defined in the inertial coordinate system Σ shown in Fig. 1(a). In addition, because the nozzle unit had four active nozzles (four degrees of freedom (DOF)), the torsional torque τ_i^{t} of nozzle unit i was controlled using a proportional derivative controller for the twist angle [16].

The rotating nozzle angles ϕ_{i1-i4} were determined to realize $\boldsymbol{f}_i$ and τ_i^{t}, and the nozzle angles were realized using servo motors. Although the relationship between ϕ_{i1-i4} and $(\boldsymbol{f}_i, \tau_i^{\mathrm{t}})$ is nonlinear, we can calculate ϕ_{i1-i4} using quadratic programming [16] in the following moving range:

$$0° \leqq \phi_{i1,i2} \leqq 180°, -90° \leqq \phi_{i3} \leqq 75°, -75° \leqq \phi_{i4} \leqq 90°.$$

C. Problems of Conventional Control Methods

The conventional control method cannot effectively suppress the vibrations caused by the mobile base because it assumes the fixed root. In the preliminary experiments, the pitch postures of the robot, especially the head nozzle, often vibrated when the mobile base changed its translational acceleration to move forward or backward. Particularly, if the posture of the nozzle unit vibrated significantly owing to robot vibrations, nozzle units sometimes caused the saturation of the reaction forces because the moving ranges of the injection nozzles were limited. The inability to achieve a net force to fly increased the risk of falling.

Thus, in this study, we designed a new controller to dampen the vibration of the robot, particularly the pitch posture vibration of the nozzle unit, against the forward and backward movement of the mobile base without the control input or sensing values of the mobile base. Specifically, we focus on the planar movement on a vertical plane.

IV. MODEL AND CONTROLLER

A. Robot Model With a Mobile Base

To design and evaluate the controller, a model of a flexible body connected to a mobile base in the sagittal plane was developed, as shown in Fig. 2, by improving the conventional model with a fixed root [11], [17]. The model was based on the following assumptions:

- The flexible body was approximated by a multi-link rigid body connected by elastic joints as [11], which is discrete and amenable to apply the $\mathcal{H}_\infty$ controller.
- The reaction forces generated by nozzle units were modeled as external forces on links' center of mass (CoM).
- To simulate a mobile base, the root joint was assumed to have horizontal degrees of freedom x_0. Furthermore, the position of the root joint was treated as a constraint in the
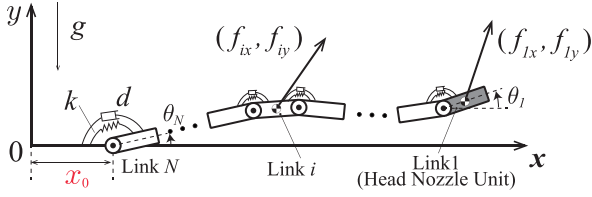
Fig. 2.   Model of a continuum robot with a mobile base.

Fig. 3.   Block diagram of $\mathscr{H}_\infty$ control.

model because the actual mobile base is sufficiently heavy relative to the continuum body.

- Because the actual body had a bending tendency, the natural angle of the springy joint was parameterized.
- As the effect of the flowing fluid inside the hose, we considered only the weight while ignoring the momentum.

Under these assumptions, we designed a model comprising N rigid-body uniform links in the x–y plane, as shown in Fig. 2. Links 1...N approximate the continuum body (mass of link i:m_i, length:l, inertial moment:I_i, and pitch angle:θ_i). Each joint i has elastic and damping elements, whose spring stiffness and damping coefficients are k and d, respectively. In addition, we set the neutral angle of the elastic joint i to ϕ_{oi} as the bending tendency. The CoM of each link is denoted as (x_i^c, y_i^c). The applied external force is denoted by (f_{xi}, f_{yi}) (if the link does not correspond to the nozzle unit, the force is set to zero). The last joint can move in the x-direction (the position is denoted as x_0). The acceleration due to gravity is denoted by g.

The vectors $\boldsymbol{x}^c, \boldsymbol{y}^c, \boldsymbol{m}, \boldsymbol{f}_x,$ and $\boldsymbol{f}_y (\in \mathbb{R}^{N \times 1})$ have elements $x_i^c, y_i^c, m_i, f_{xi}$ and f_{yi}, respectively. The vectors $\boldsymbol{I}, \boldsymbol{\theta}, \boldsymbol{\phi}_o (\in \mathbb{R}^{N \times 1})$ are defined with the elements I_i, θ_i, ϕ_{oi}, respectively. The generalized coordinate $\boldsymbol{q}$ of the model is $[\boldsymbol{\theta}^T \ x_0]^T$.

Based on a procedure similar to [11], the equation of motion can be derived as follows:

$$H\ddot{\boldsymbol{\theta}} + Q\dot{\boldsymbol{\theta}} + \boldsymbol{g}_s + \ddot{x}_0\boldsymbol{\tau}_D = T_x\boldsymbol{f}_x + T_y\boldsymbol{f}_y \qquad (2)$$

where $H(\boldsymbol{\theta})$ is an innertia matrix (regular matrix), $Q(\boldsymbol{\theta}, \dot{\boldsymbol{\theta}})\dot{\boldsymbol{\theta}}$ is the term of Coriolis and centrifugal forces, $\boldsymbol{g}_s(\boldsymbol{\theta})$ is the term of gravity and springy forces, and the term $\ddot{x}_0\boldsymbol{\tau}_D(\boldsymbol{\theta})$ represents the torque disturbance on the joints caused by the mobile base motion $\ddot{x}_0$. $T_x(\boldsymbol{\theta})\boldsymbol{f}_x$ and $T_y(\boldsymbol{\theta})\boldsymbol{f}_y$ represent the generalized torques transformed from the external forces in x and y directions, respectively. Concrete formulations of $H, Q, \boldsymbol{g}_s, \boldsymbol{\tau}_D, T_x$ and T_y are shown in Appendix.

B. Overview of the Proposed Controller

The proposed controller combines the conventional and linear controllers. When there is no disturbance, the equations of motion are the same as those in the conventional case. In this case, the conventional controller (1) can generate stable equilibrium points in the nonlinear system [17]. Thus, assuming that the disturbance is small, we can linearize the system with respect to the equilibrium points to apply a linear controller. We selected $\mathscr{H}_\infty$ controller as the linear controller to suppress a vibration against periodic mobile base's disturbance. The combination with the conventional controller enables us to use the well-established linear control method under the linearization assumptions.

Particularly, we controlled the net force of the nozzle unit $\vec{f}_i = [f_{xi}, f_{yi}]^T$ (i is the link number of the nozzle unit) as follows:

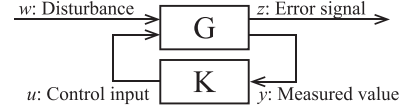$$\vec{f}_i = \vec{F}_i - D_i\vec{v}_i + \vec{u}_i \qquad (3)$$

where $\vec{F}_i = [F_{xi}, F_{yi}]^T$ is the constant force vector, $\vec{v}_i = [\dot{x}_i^c, \dot{y}_i^c]^T$ is the velocity of the CoM of link i, and D_i is a diagonal matrix with component s_i. The first and second terms are the same as those of conventional control, and the third term $\vec{u}_i$ is the control input for the $\mathscr{H}_\infty$ controller. Particularly, because the head nozzle unit vibrates severely, we only consider the input of the head nozzle unit $\vec{u}_1$ ($\vec{u}_i = \vec{0}$ for $i \neq 1$). This target net force $\vec{f}_i$ is realized by commanding four rotating nozzle angles to the servomotors on the nozzle unit, as explained in Section III-B.

C. Linearization of the System

Substituting $\vec{f}_i$ in (3) into the equation of motion (2), we obtain the following form:

$$\dot{\boldsymbol{X}} = \boldsymbol{h}(\boldsymbol{X}, \boldsymbol{F}_x, \boldsymbol{F}_y) + E\ddot{x}_0 + V\boldsymbol{u} \qquad (4)$$

where $\boldsymbol{X} = [\boldsymbol{\theta}^T \ \dot{\boldsymbol{\theta}}^T]^T$ is the state vector, $\boldsymbol{u} = [u_{1x} \ u_{1y}]^T$ is the control input, and $\boldsymbol{h}$ is a function of $\boldsymbol{X}$. E and V are expressed as follows:

$$E = \begin{bmatrix} \boldsymbol{0}_{N \times 1} \\ H^{-1}\boldsymbol{\tau}_D \end{bmatrix}, \ V = \begin{bmatrix} \boldsymbol{0}_{N \times 1} & \boldsymbol{0}_{N \times 1} \\ H^{-1}T_x\boldsymbol{e}_0 & H^{-1}T_y\boldsymbol{e}_0 \end{bmatrix},$$

where $\boldsymbol{e}_0 = \begin{bmatrix} 1 & 0 & \cdots & 0 \end{bmatrix}^T$. $\boldsymbol{X}^*$ satisfying $\boldsymbol{h}(\boldsymbol{X}^*, \boldsymbol{F}_x, \boldsymbol{F}_y) = \boldsymbol{0}$ is the equilibrium point of the conventional system (for $\ddot{x}_0 = 0$, $\boldsymbol{u} = \boldsymbol{0}$). By assuming that $\ddot{x}_0$ and $\boldsymbol{u}$ are small, we take an approach to linearize the system (4) around $\boldsymbol{X}^*$ by ignoring the quadratic terms. Using the deviation $\boldsymbol{x} = [\delta\boldsymbol{\theta}^T \ \delta\dot{\boldsymbol{\theta}}^T]^T$ ($\boldsymbol{X} = \boldsymbol{X}^* + \boldsymbol{x}$), the linearized equation can be written as

$$\dot{\boldsymbol{x}} = A\boldsymbol{x} + E^*\ddot{x}_0 + V^*\boldsymbol{u}, \qquad (5)$$

where E^* and V^* denote the matrices E and V when $\boldsymbol{X} = \boldsymbol{X}^*$, respectively. Matrix A is the Jacobian matrix around the equilibrium point $\boldsymbol{X}^*$ and is defined by the following equation:

$$A = \left. \frac{\partial \boldsymbol{h}}{\partial \boldsymbol{X}} \right|_{\boldsymbol{X} = \boldsymbol{X}^*}$$

Because we cannot analytically derive $\boldsymbol{X}^*$ as in [17], matrix A is numerically calculated in this study.

D. $\mathscr{H}_\infty$ Controller

The $\mathscr{H}_\infty$ controller is a linear robust control method [12]. Consider a plant G and a controller K as Fig. 3. Let the control input, measured value, disturbance input, and error signal for G to be $\boldsymbol{u}, \boldsymbol{y}, \boldsymbol{w}$ and $\boldsymbol{z}$, respectively. The state–space representation of plant G is set as follows:

$$\dot{\boldsymbol{x}} = A\boldsymbol{x} + \begin{bmatrix} B_1 & B_2 \end{bmatrix} \begin{bmatrix} \boldsymbol{w} \\ \boldsymbol{u} \end{bmatrix},$$

$$\begin{bmatrix} \boldsymbol{z} \\ \boldsymbol{y} \end{bmatrix} = \begin{bmatrix} C_1 \\ C_2 \end{bmatrix} \boldsymbol{x} + \begin{bmatrix} D_{11} & D_{12} \\ D_{21} & D_{22} \end{bmatrix} \begin{bmatrix} \boldsymbol{w} \\ \boldsymbol{u} \end{bmatrix} \qquad (6)$$

where $\boldsymbol{x}$ is the state variable of G. The state–space representation of controller K is set as $\dot{\boldsymbol{x}}_K = A_K \boldsymbol{x}_K + B_K \boldsymbol{y}, \ \boldsymbol{u} = C_K \boldsymbol{x}_K$, where $\boldsymbol{x}_K$ is the state variable of K. The problem of deriving $\mathscr{H}_\infty$ controller is to specify controller K (i.e., state-space matrices A_K, B_K, and C_K) to minimize the $\mathscr{H}_\infty$ norm of the closed-loop transfer matrix from disturbance input $\boldsymbol{w}$ to error signal $\boldsymbol{z}$ (output). Intuitively, in the case of a single-input and single-output system, because the $\mathscr{H}_\infty$ norm gives the maximum amplification of an input signal at the output in the frequency domain (i.e., the maximum gain in the Bode diagram of the corresponding transfer function), the $\mathscr{H}_\infty$ controller can suppress the amplification of disturbance input $\boldsymbol{w}$ at error signal $\boldsymbol{z}$, which is feasible for suppressing the pitch vibration against the disturbance as the mobile base movement. This problem can be numerically solved, for example, using the two-Reccati formulae method [18], [19], and MATLAB also provides the solver [20].

E. Implementation of the $\mathscr{H}_\infty$ Controller to Our Linearized System

Based on (5), we specify the variables of plant G as follows. $\boldsymbol{x}, \boldsymbol{u}$ and A in (6) are the same as those discussed in (5). $\boldsymbol{w}$ corresponds to $\ddot{x}_0$ in (5) because the disturbance input is the movement of the mobile base. $\boldsymbol{z}$ is set as the posture displacement of the head nozzle $\delta\theta_1$. This is because the head nozzle unit vibrates excessively in the preliminary experiments. $\boldsymbol{y}$ is set as the velocity of the head and middle nozzles $\boldsymbol{y} = \begin{bmatrix} \dot{x}_1^c & \dot{y}_1^c & \dot{x}_j^c & \dot{y}_j^c \end{bmatrix}^T$, where j is the index of the link of the middle nozzle. From (2) and (5), each matrix in (6) can be expressed as follows:

$$B_1 = E^*, \ B_2 = V^*, \ C_1 = \begin{bmatrix} 1 & 0 & \cdots & 0 \end{bmatrix} (\in \mathbb{R}^{1 \times 2N}),$$

$$C_2 = \begin{bmatrix} \mathbf{0}_{N \times 1} & \mathbf{0}_{N \times 1} & \mathbf{0}_{N \times 1} & \mathbf{0}_{N \times 1} \\ T_x^T \boldsymbol{e}_0 & T_y^T \boldsymbol{e}_0 & T_x^T \boldsymbol{e}_j & T_y^T \boldsymbol{e}_j \end{bmatrix}^T \quad (7)$$

where $\boldsymbol{e}_j \in \mathbb{R}^{N \times 1}$ is a unit vector whose j-th element is one. D_{11}, D_{12}, D_{21}, and D_{22} are zero matrices of $1 \times 1, 1 \times 2, 4 \times 1$, and 4×2, respectively.

F. Numerical Calculation of Controller K

Controller K is numerically calculated for each equilibrium point using the *hinfsyn* function in MATLAB. The function calculates state-space matrices A_k, B_k, and C_k to minimize the $\mathscr{H}_\infty$ norm.

We slightly modified plant G to apply the *hinfsyn* function. The *hinfsyn* function requires the following conditions to be satisfied [20]: (1): (A, B_2) is controllable, (2):(C_2, A) is observable, (3):D_{12} is the column full rank, and (4):D_{21} is the row-full rank. Although Conditions (1) and (2) are fulfilled (numerically confirmed for all targeted equilibrium points), Conditions (3) and (4) are not satisfied because D_{12} and D_{21} are zero matrices. Therefore, we redefine D'_{12} and D'_{21} by adding temporary disturbance inputs (w_1, w_2, w_3, w_4) and error outputs (z_1 and z_2) with constants ϵ_w and ϵ_z as follows:

$$D'_{12} = \begin{bmatrix} 0 & \epsilon_z & 0 \\ 0 & 0 & \epsilon_z \end{bmatrix}^T, \ D'_{21} = \begin{bmatrix} \mathbf{0}_{4 \times 1} & \mathrm{diag}(\epsilon_w, \epsilon_w, \epsilon_w, \epsilon_w) \end{bmatrix}$$

This also makes $\boldsymbol{w}' = [\boldsymbol{w}^T \ w_1 \ w_2 \ w_3 \ w_4]^T \in \mathbb{R}^5, \ \boldsymbol{z}' = [\boldsymbol{z}^T \ z_1 \ z_2]^T \in \mathbb{R}^3$ and $D'_{11} = \mathbf{0}_{3 \times 5}$. We set ϵ_w and ϵ_z to sufficiently small values for 0.1.
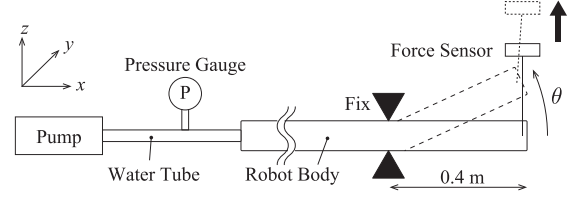

Fig. 4. Parameter identification experiments using a universal test machine.

After the *hinfsyn* function calculated the controller K (matrices $A_k \in \mathbb{R}^{2N \times 2N}, B_k \in \mathbb{R}^{2N \times 4}$, and $C_k \in \mathbb{R}^{2 \times 2N}$), we lowered the dimensions of controller K to prevent an increase in the computational complexity. We used the balanced truncation model-reduction method with MATLAB to decrease the number of dimensions. We discarded states with Hankel singular values less than one-tenth of the maximum value.

V. PARAMETER IDENTIFICATION

Considering that the mass, length, and moment of inertia of the body can be obtained through actual measurements or calculations, spring stiffness k, damping coefficient d, and bending tendency $\boldsymbol{\phi}_o$, which are the properties of the joint of the body, are identified in this section.

A. Identification of the Spring Stiffness

The spring stiffness was derived using the relationship between the force and pitch angle when a part of the flexible body was pulled and displaced in an experiment. The internal water pressure was varied in the experiment to investigate its effect on the spring stiffness.

1) Method: The configuration of the experimental equipment is discussed in Fig. 4. The robot was anchored 0.4 m from the head and hooked by a string on the head. The water inside the hose was pressurized using a pump at the base. A universal testing machine pulled the string at the top. The string's tension was measured using a customized force sensor (*Leptrino*), and the head pitch angle θ was measured using an IMU sensor attached to the head. Water pressure was measured using a pressure gauge (GP-M250T, *Keyence*).

The experimental procedure was as follows: Initially, the head of the robot was horizontal and the string was pulled up to a specific displacement (d) at a constant speed of 15 mm/s. The displacement was then maintained for 60 s. Subsequently, the displacement was returned to zero at the same velocity, and then the head remained stationary for 30 s. Seven displacements d ranging from 0.14 m to 0.02 m and three pressures of 0.14, 0.29, and 0.45 MPa were used. Five experiments were conducted under each condition.

The model used to estimate the spring stiffness is described as follows: The test target was modeled as a uniform rigid link (length l and mass m) with a rotating spring joint (spring stiffness k) at a fixed part. Let θ be the attitude when external forces F_x and F_z are exerted on the tip. The moment equilibrium equation is expressed as

$$-F_x l \sin\theta + F_z l \cos\theta - \frac{1}{2} mgl \cos\theta = k\theta \quad (8)$$
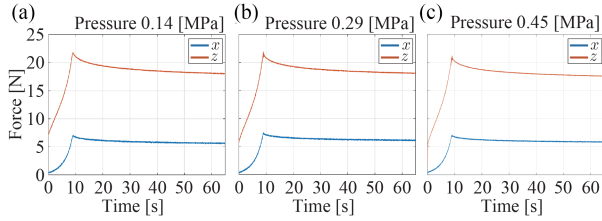
Fig. 5. Time responses of the holding force at various pressures ((a) 0.14, (b) 0.29, and (c) 0.45 MPa) (one example). The tip displacement increases from 0 to 9.3 s, and is then held for 60 s. This graph shows the stress-relaxation property.
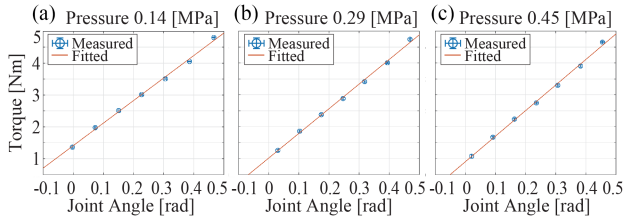

Fig. 6. Relationship between the torque and pitch angle θ for various pressures ((a) 0.14, (b) 0.29, and (c) 0.45 MPa). Points represent the mean measured values, and the line represents the fitting line. We can observe a linear relation.

Variables l and m were measured in advance. The variables θ, F_x, and F_z can be measured using a force sensor and IMU. Therefore, k can be estimated from (8).

2) Results: The time responses of the holding force (Fig. 5) show that the flexible body has a stress-relaxation property, in which the force gradually decreases under constant displacement (from 9.3 s to 60 s). This was the case for all displacements at various pressures. Because this study attempted to suppress the vibration for a short period (approximately 1 s), it was unnecessary to explicitly consider the effects of stress relaxation. Therefore, the spring stiffness was estimated from the force value at the peak.

Then, using the measured θ, F_x, F_z, the relationship between the left side of (8) (applied torque at the joint) and the pitch angle (θ) is shown in Fig. 6. Although the torque was not zero when the joint angle was zero, we observed a linear relationship between the pitch angle and torque displacement at each pressure (Fig. 6). The gradient of the fitting line using the linear regression method is regarded as the spring stiffness k in the model, and its value is calculated as 7.06 Nm/rad at 0.14 MPa, 7.73 Nm/rad at 0.29 MPa, and 8.02 Nm/rad at 0.45 MPa. Spring stiffness increased with increasing pressure.

From the results, we conclude that the rigid-link model can approximate the relationship between the force and displacement of the continuum body < 0.5 rad pitch angle displacement for a 0.4-m-long body. Although the torque was not zero when the joint angle was zero, there was a bending tendency on the robot owing to the viscoelastic properties of the robot body (made of rubber and polypropylene), which offset the torque. In addition, the spring stiffness changed with the pressure. This was attributed to the tube expansion caused by the internal water pressure. Based on this experiment, the spring stiffness was identified as 8.02 Nm/rad at 0.45 MPa, which is the closest to the pressure in the flying experiment.

TABLE I
PHYSICAL PARAMETERS USED IN THE DAMPING ESTIMATION

Element	Value	Element	Value
N	10	m_1 [kg]	3.11
k [Nm/rad]	8.02	m_6 [kg]	3.01
ϕ_{o1-o10} [rad]	estimate	$m_{2-5,7-10}$ [kg]	0.70
m [kg]	0.4	I_1 [kg·m^2]	0.017
l [m]	0.2	I_6 [kg·m^2]	0.016
g [m/s^2]	9.8	$I_{2-5,7-10}$ [kg·m^2]	0.0095

B. Identification of the Damping Coefficient

A Bode diagram of the change in the pitch angle in the head nozzle unit was generated by periodically vibrating the root cart. Bending tendency ϕ_o and damping coefficient d were identified by comparing the Bode diagrams obtained from the actual system and the simulation.

1) Method: To create a Bode diagram using the actual system, a sinusoidal acceleration input was applied to the root cart while the system flew stably in an equilibrium shape with the conventional controller. After the head nozzle unit vibration reached a steady state, the cart acceleration and pitch angle of the head nozzle unit were measured using the IMU sensor. A discrete Fourier transform (DFT) analysis of approximately 15 s of measurements from both sensors was performed to obtain the amplitude components corresponding to the input frequency. The amplitude of the pitch angle of the nozzle unit was divided by the acceleration amplitude, which was non-dimensionalized by the gravity acceleration g, to obtain the gain, and a Bode diagram was created. The constant force inputs and D-gains added to each nozzle unit (1) were $\vec{F}_1 = [9.96, 9.96]^T$, $\vec{F}_j = [4.37, 15.7]^T$ N, $s_1 = 4.0$, and $s_j = 2.0$ N/(m/s), where j represents the middle nozzle unit.

To compare the experimental results, Bode diagrams were obtained through dynamic simulations using the same procedure as that used in the experiment. The acceleration of the cart was input into $\ddot{x}$ of the equation of motion (2), and the force input $\boldsymbol{f}_{x,y}$ was determined using the conventional controller ($\vec{u} = 0$ in (3)). As in the actual system, the nozzle unit model and jet-nozzle angle-determination method proposed in [16] were used to determine the force input $\boldsymbol{f}_{x,y}$, considering the nozzle-operating range. The total number of links was $N = 10$, and the nozzle units corresponded to links 1 and 6 ($j = 6$). The physical parameters are listed in Table I. The head of the actual robot was fixed to the body at approximately 53 deg (0.88 rad) downward. The physical parameters for joint 1 in the model were reproduced by setting $k = 1000$ Nm/rad, $d = 8.21$ Nm/(rad/s) (critical damping), and $\phi_{o1} = -53$ deg (-0.88 rad).

In this experiment, damping coefficient d and the bending tendency were estimated. Because the body was approximately a suspension curve when it flew, bending tendency ϕ_o was assumed to be a curve with a constant curvature of ϕ [deg] per link (excluding the fixed part with the nozzle unit).

2) Result: The obtained Bode diagrams are shown in Fig. 7. Fig. 7(a) shows several simulation results obtained when only the bending curvature ϕ changes, and Fig. 7(b) shows the simulation results when only the damping coefficient d changes. A peak of the experimental Bode plot was observed at approximately 1.3 Hz with a gain of approximately 5 dB.

The bending curvature and damping coefficients were determined based on these results. Fig. 7(a) shows that as the bending curvature ϕ increases, the frequency of the maximum
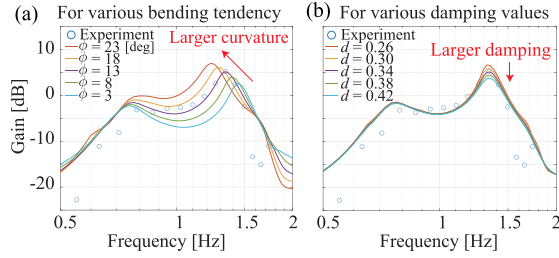
Fig. 7. Changes in the Bode diagram for different bending tendencies and damping coefficients compared with experimental results.
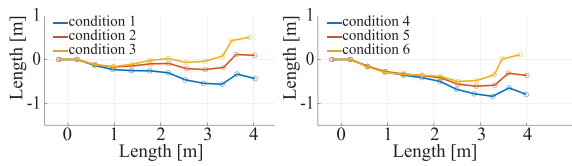

Fig. 8. Six shapes for controller verification.

peak tends to decrease, and the magnitude of the peak gain tends to increase. The results in Fig. 7(b) show that as the damping coefficient d increases, only the maximum peak gain decreases. From this, the bending curvature was determined such that the maximum peak frequency agreed with the experimental results (ϕ=13 deg), and the damping coefficient was determined such that the magnitude of the maximum gain agreed with the experimental results (d=0.34 Nm/(rad/s)). The Bode diagram of the identified parameters corresponds to the purple line shown in Fig. 7.

Furthermore, the Bode diagram of the model with the identified parameters was in good qualitative agreement with the experimental results, even outside the peaks. This result demonstrates the validity of the proposed model. Therefore, the method used to determine the proposed model and spring stiffness is considered appropriate.

VI. VERIFICATION OF THE PROPOSED CONTROLLER

A. Targeted Robot and Shape

The target robot used is the same as previously described. However, the bending tendency estimated in the previous section was more accurately estimated based on the shape in actual flight (the details have been omitted because they are not relevant to this study). The obtained bending tendency values were $\phi_o = (-0.88, 1.14, 0.59, 0.7, 0.11, 0.18, -0.19, -0.4, -0.89, 1.81)$ rad. The other physical parameters were the same as those listed in Table I.

Because the frequency response changed depending on the shape, six shapes (Fig. 8) corresponding to the middle-nozzle unit positions (top and bottom) and head-nozzle unit positions (top, middle, and bottom) were included in the analysis. The constant force vectors (F_{1x}, F_{1y}), (F_{6x}, F_{6y}) for the six shapes are listed in Table II.

TABLE II
CONSTANT FORCE INPUT TO EACH NOZZLE UNIT FOR SIX SHAPES

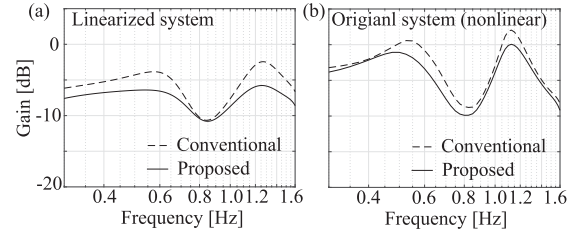| Shape	F_{1x} [N]	F_{1y} [N]	F_{6x} [N]	F_{6y} [N]
1	9.96	9.96	4.37	15.7
2	8.36	11.5	3.42	15.9
3	5.99	12.3	2.60	15.7
4	11.3	8.94	7.11	14.0
5	8.94	11.0	6.67	13.2
6	5.36	12.3	6.48	12.7

Fig. 9. Bode diagrams with and without the $\mathscr{H}_\infty$ controller for Shape 1; (a) and (b) show the results obtained with the linear system and the dynamic simulation, respectively.

TABLE III
MAXIMUM PEAK FREQUENCY AND GAIN FOR SIX SHAPES

Shape	Linear system			Nonlinear system		
	Peak freq	Prv. ctr. gain	$\mathscr{H}_\infty$ ctr. gain	Peak freq	Prv. ctr. gain	$\mathscr{H}_\infty$ ctr. gain
1	1.27	-2.44	-5.79	1.12	2.04	0.05
2	1.16	-2.00	-5.00	1.03	1.12	-1.77
3	1.04	-1.47	-4.34	0.85	1.28	-2.74
4	1.39	-3.99	-6.74	1.33	-1.73	-3.86
5	1.23	-4.64	-7.11	1.15	-2.70	-4.90
6	1.01	-6.01	-8.85	0.90	-4.06	-5.75

B. Designing an $\mathscr{H}_\infty$ Controller and Linear Bode Diagram

For each shape, a controller was designed based on Section IV-E. We reduced the order of controller K for each shape based on Section IV-E. The dimension of K was determined to six, six, five, six, six, and five for each of the six shapes, respectively.

Fig. 9(a) compares the Bode diagrams of the conventional and $\mathscr{H}_\infty$ controller on shape 1 in the linear system (6). Two peaks were observed within the frequency band of interest. The magnitude of the peak gain can be reduced by approximately 3.5 dB using $\mathscr{H}_\infty$ control.

The left side of Table III summarizes the maximum peak frequency [Hz] and gain [dB] with and without $\mathscr{H}_\infty$ control for the six shapes. Although the peak frequency and gain vary depending on the shape, the maximum peak gain can be suppressed by approximately 3 dB in all cases.

C. Verification by Dynamic Simulation

1) Method: The obtained controller was verified in the dynamic simulation as described in Section V-B, which considered the operating range of the jet nozzle. The frequency range was set as 0.3–1.8 Hz, which is the range that can be achieved in an actual system. The amplitude of the sinusoidal input applied to the root mobile unit in the dynamics simulation was set to 1.0 m/s². Bode diagrams were created for the $\mathscr{H}_\infty$ and conventional controllers.
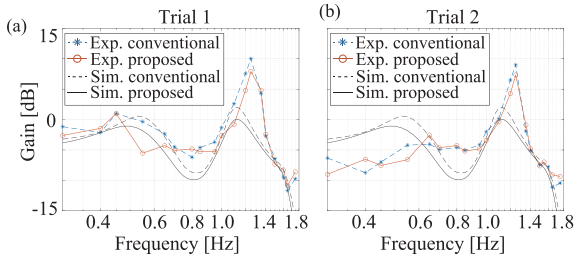
Fig. 10. Comparison of frequency responses (Bode diagrams) obtained from experiments with dynamics simulations; (a) and (b) show the results of different trials. Orange and blue points show the experimental results obtained with and without the $\mathscr{H}_\infty$ controller, respectively. Normal and dotted black lines represent the simulation results with and without the $\mathscr{H}_\infty$ controller, respectively.

2) Results: Similar to the linear system, a dynamic simulation of the nonlinear system showed that the magnitude of the peak gain could be reduced by approximately 2–3 dB in the case of Shape 1 (Fig. 9(b)). Although the shape of the Bode diagram was qualitatively similar between the linear system and dynamic simulation, the magnitude of the gain was larger in the simulation. This is because the dynamic simulation of the nonlinear system considered the motion limit of the jet nozzle. When the vibration increased, the jet nozzle entered the motion limit, and the required net force was not realized; thus, the vibration could not be suppressed compared with that of the ideal linear system.

The right side of Table III compares the maximum peak frequency [Hz] and maximum peak gain [dB] for the six shapes tested in this study, with and without $\mathscr{H}_\infty$ control. The maximum peak gain can be suppressed to approximately less than 0.05 dB (maximum reduction of approximately 4 dB) by $\mathscr{H}_\infty$ control, indicating the method's validity.

D. Verification Using an Actual System

The verification was conducted using an actual system. In the experiment, Shape 3, shown in Table 8, was targeted. As in the estimation of the damping coefficients (Section V-B), a sinusoidal acceleration input was applied to the root cart during stable flying, and time responses of the cart acceleration and the head nozzle posture were recorded. The inputs with 19 frequencies in the range of 0.32–1.73 Hz were applied. Vibrations were performed for 20 s with and without $\mathscr{H}_\infty$ control for each frequency; two trials were conducted. A DFT analysis was then performed using the method described in Section V-B to obtain the gain for each frequency. The proposed controller was implemented with a 100 Hz control frequency.

The obtained Bode diagrams are shown in Fig. 10. Figure A and B show the results of the first and second trials, respectively. The black lines are the results of the simulations discussed in the previous section, the dotted lines represent the results obtained without the proposed control, and the solid lines represent the results obtained with the proposed $\mathscr{H}_\infty$ control.

Fig. 10(a) and (b) show that the proposed controller reduces the gain by approximately 3 dB for a maximum peak at approximately 1.25 Hz, similar to the simulation results, indicating the validity of the $\mathscr{H}_\infty$ control. In addition, the response is similar to that of the dynamic simulation in the presence of peaks at approximately two locations. The Bode plot in the range of
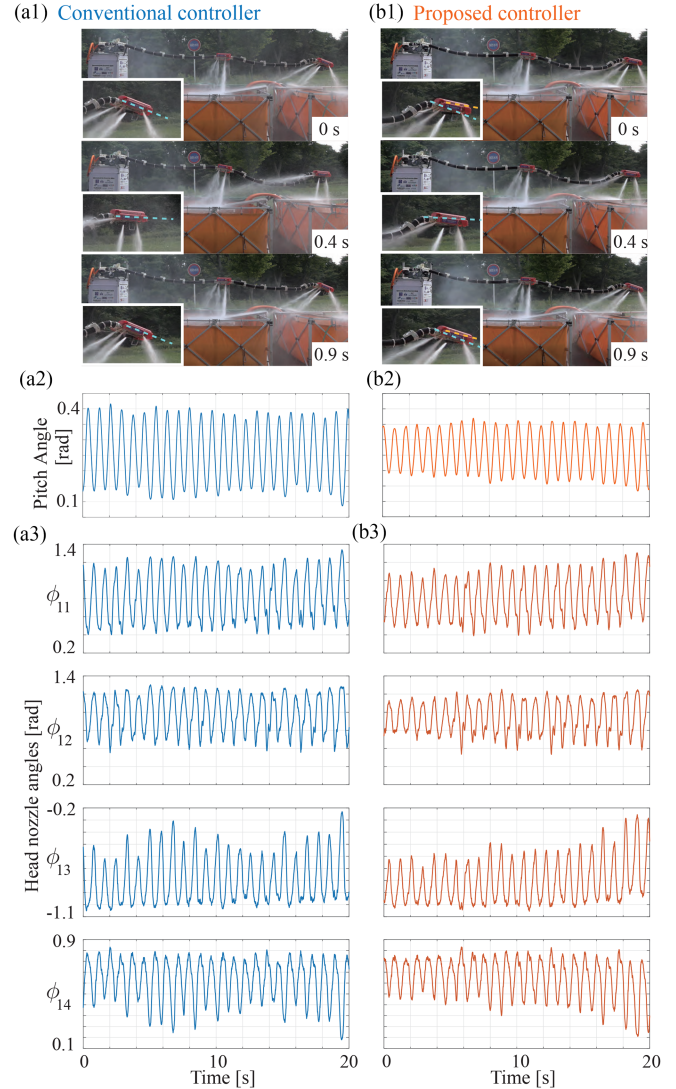

Fig. 11. Difference in pitch vibrations of the head nozzle unit with (b1,2) and without the proposed $\mathscr{H}_\infty$ control (a1,2). Time responses of the four nozzle angles of the head nozzle unit with (b3) and without the proposed $\mathscr{H}_\infty$ controller (a3).

0.3–0.7 Hz slightly changed depending on the trial, and this was possibly owing to the wind effect and the change in the bending tendency. Because this experiment took approximately 30 min, the bending tendency changed over time. Further, the low-frequency data presented in Fig. 10(b) was taken around the end of the experiment, and the effect of the bending tendency change could be more significant. Thus, the proposed model adequately represents the critical behavior of the actual system.

The time responses of the head nozzle pitch angle (Fig. 11(a1), (a2), (b1), and (b2)) and the four jet-nozzle angles (Fig. 11(a3) and (b3)) at the peak frequency of the first trial data were compared between the proposed $\mathscr{H}_\infty$ and conventional controllers. Fig. 11(a) and (b) correspond to the proposed and conventional controls, respectively.

Fig. 11(a1), (a2), (b1), and (b2) show that the amplitude of the nozzle posture is reduced by approximately 32% in the proposed $\mathscr{H}_\infty$ controller, compared to the conventional

controller. Furthermore, from Fig. 11(a3) and (b3), the amplitudes of rotating nozzle angles were also reduced by approximately 16–18%, compared to conventional nozzle angles. The amplitude-reduction ratio was calculated using DFT analysis. We compare the amplitudes of elements related to the input frequency. Introducing the proposed $\mathscr{H}_\infty$ controller decreased the risk of reaching the movable limit of the nozzle under a disturbance. The proposed $\mathscr{H}_\infty$ controller enabled the nozzle unit to achieve a net force and stable flying, even under a larger disturbance input.

VII. CONCLUSION

This is the first study to propose a translational disturbance rejection method for jet-actuated flying continuum robots on a mobile base without control inputs or sensing information from the mobile base. First, a 2D model was created considering a mobile unit. We designed a disturbance-rejection controller using the $\mathscr{H}_\infty$ method to suppress the vibration of the head of the DFF against the acceleration of the mobile base. Subsequently, the robot parameters were identified from tensile tests and dynamic excitation experiments, verifying that our model agreed well with the experimental results. Finally, the proposed controller was verified using simulations and experiments with a 4-m-long continuum robot. Experiments with the robot showed that the $\mathscr{H}_\infty$ controller decreased the peak gain against the disturbance by approximately 3 dB, which increased the range for nozzle injection by 16%.

In the future, other disturbances, such as the wind, vertical base movement, and three-dimensional shape changes, should be considered. In addition, a method is required to estimate and deal with the bending tendency, which can change with the time history of the robot's movement.

APPENDIX A

$$H = S\overline{M}S + C\overline{M}C + J,$$

$$Q = (S\overline{M}C - C\overline{M}S)\mathrm{diaXg}(\dot{\boldsymbol{\theta}}) + dR^T R$$

$$\boldsymbol{g}_\mathrm{s} = lgCA^T\boldsymbol{m} + kR^T(R\boldsymbol{\theta}\boldsymbol{\phi}),$$

$$\boldsymbol{\tau}_\mathrm{D} = SB^T lM\boldsymbol{e}_x, \ T_x = -lSB^T,$$

$$T_y = lCB^T, \ \overline{M} = l^2 B^T MB, \ M = \mathrm{diag}(\boldsymbol{m}), \ J = \mathrm{diag}(\boldsymbol{I}),$$

$$S = \mathrm{diag}(\sin\theta_1, \dots, \sin\theta_N), \ C = \mathrm{diag}(\cos\theta_1, \dots, \cos\theta_N),$$

$$B = \begin{bmatrix} 1/2 & 1 & \cdots & 1 \\ 0 & 1/2 & \cdots & 1 \\ \vdots & \vdots & \ddots & \vdots \\ 0 & 0 & \cdots & 1/2 \end{bmatrix},$$

$$R = \begin{bmatrix} 1 & -1 & \cdots & 0 \\ 0 & 1 & \cdots & 0 \\ \vdots & \vdots & \ddots & \vdots \\ 0 & 0 & \cdots & 1 \end{bmatrix}$$

where $\boldsymbol{e}_x = \begin{bmatrix} 1 & \cdots & 1 \end{bmatrix}^T$ $(\in \mathbb{R}^{N \times 1})$, H is a regular matrix because $m_i > 0$ and $I_i > 0$ for all i.

REFERENCES

[1] I. D. Walker, "Continuous backbone "continuum" robot manipulators," *ISRN Robot.*, vol. 2013, 2013, Art. no. 726506.

[2] J. D. Greer, T. K. Morimoto, A. M. Okamura, and E. W. Hawkes, "Series pneumatic artificial muscles (SPAMS) and application to a soft continuum robot," in *Proc. IEEE Int. Conf. Robot. Automat.*, 2017, pp. 5503–5510.

[3] E. W. Hawkes, L. H. Blumenschein, J. D. Greer, and A. M. Okamura, "A soft robot that navigates its environment through growth," *Sci. Robot.*, vol. 2, no. 8, 2017, Art. no. aan3028.

[4] J. A. Silva Rico, G. Endo, S. Hirose, and H. Yamada, "Development of an actuation system based on water jet propulsion for a slim long-reach robot," *Robomech J.*, vol. 4, no. 1, pp. 1–17, 2017.

[5] D.-H. Lee, T. Huynh, Y.-B. Kim, and C. Soumayya, "Motion control system design for a flying-type firefighting system with water jet actuators," *Actuators*, vol. 10, no. 10, 2021, Art. no. 275.

[6] T. Huynh, D.-H. Lee, and Y.-B. Kim, "Study on actuator performance evaluation of aerial water-powered system for firefighting applications," *Appl. Sci.*, vol. 13, no. 3, 2023, Art. no. 1965.

[7] Y. Yamauchi et al., "Development of a continuum robot enhanced with distributed sensors for search and rescue," *Robomech J.*, vol. 9, no. 8, 2022, Art. no. 8.

[8] I. A. Gravagne, C. D. Rahn, and I. D. Walker, "Large deflection dynamics and control for planar continuum robots," *IEEE/ASME Trans. Mechatron.*, vol. 8, no. 2, pp. 299–307, Jun. 2003.

[9] A. Jnifene and W. Andrews, "Experimental study on active vibration control of a single-link flexible manipulator using tools of fuzzy logic and neural networks," *IEEE Trans. Instrum. Meas.*, vol. 54, no. 3, pp. 1200–1208, Jun. 2005.

[10] Y. Ambe, Y. Yamauchi, M. Konyo, K. Tadakuma, and S. Tadokoro, "Stabilized controller for jet actuated cantilevered pipe using damping effect of an internal flowing fluid," *IEEE Access*, vol. 10, pp. 5238–5249, 2022.

[11] T. Yamaguchi et al., "A mechanical approach to suppress the oscillation of a long continuum robot flying with water jets," *IEEE Robot. Automat. Lett.*, vol. 4, no. 4, pp. 4346–4353, Oct. 2019.

[12] O. H. Bosgra, H. Kwakernaak, and G. Meinsma, "Design methods for control systems," *Notes a Course Dutch Inst. Syst. Control, Winter Term*, pp. 241–288, 2007.

[13] P. K. W. Abeygunawardhana and T. Murakami, "Vibration suppression of two-wheel mobile manipulator using resonance-ratio-control-based null-space control," *IEEE Trans. Ind. Electron.*, vol. 57, no. 12, pp. 4137–4146, Dec. 2010.

[14] B. Nilsson, J. Nygårds, U. Larsson, and Å. Wernersson, "Control of flexible mobile manipulators: Positioning and vibration reduction using an eye-in-hand range camera," *Control Eng. Pract.*, vol. 7, no. 6, pp. 741–751, 1999.

[15] M. Rigotti-Thompson, M. Torres-Torriti, F. A. Auat Cheein, and G. Troni, "$\mathscr{H}_\infty$-based terrain disturbance rejection for hydraulically actuated mobile manipulators with a nonrigid link," *IEEE/ASME Trans. Mechatron.*, vol. 25, no. 5, pp. 2523–2533, Oct. 2020.

[16] H. Ando et al., "Fire extinguishment using a 4m long flying-hose-type robot with multiple water-jet nozzles," *Adv. Robot.*, vol. 34, no. 11, pp. 700–714, 2020.

[17] H. Ando et al., "Aerial hose type robot by water jet for fire fighting," *IEEE Robot. Automat. Lett.*, vol. 3, no. 2, pp. 1128–1135, Apr. 2018.

[18] K. Glover and J. C. Doyle, "State-space formulae for all stabilizing controllers that satisfy an H∞-norm bound and relations to relations to risk sensitivity," *Syst. Control Lett.*, vol. 11, no. 3, pp. 167–172, 1988. [Online]. Available: https://www.sciencedirect.com/science/article/pii/0167691188900552

[19] J. Doyle, K. Glover, P. Khargonekar, and B. Francis, "State-space solutions to standard H₂ and H∞ control problems," in *Proc. IEEE Amer. Control Conf.*, 1988, pp. 1691–1696.

[20] The MathWorks, Inc., "hinfsyn: Compute H-infinity optimal controller," Accessed: Jul. 26, 2023. [Online]. Available: https://www.mathworks.com/help/robust/ref/dynamicsystem.hinfsyn.html